

Reaction coordinate flows for model reduction of molecular kinetics

Hao Wu^{*1,2} and Frank Noé^{*3,4,5}

¹*School of Mathematical Sciences, Institute of Natural Sciences and MOE-LSC, Shanghai Jiao Tong University, Shanghai, P. R. China*

²*School of Mathematical Sciences, Tongji University, Shanghai, P. R. China*

³*Department of Mathematics and Computer Science and Department of Physics, Freie Universität Berlin, Berlin, Germany*

⁴*Department of Chemistry, Rice University, Houston, TX, USA*

⁵*Microsoft Research AI4Science, Berlin, Germany*

(*Authors to whom correspondence should be addressed: hwu81@sjtu.edu.cn and frank.noe@fu-berlin.de)

In this work, we introduce a flow based machine learning approach, called reaction coordinate (RC) flow, for discovery of low-dimensional kinetic models of molecular systems. The RC flow utilizes a normalizing flow to design the coordinate transformation and a Brownian dynamics model to approximate the kinetics of RC, where all model parameters can be estimated in a data-driven manner. In contrast to existing model reduction methods for molecular kinetics, RC flow offers a trainable and tractable model of reduced kinetics in continuous time and space due to the invertibility of the normalizing flow. Furthermore, the Brownian dynamics-based reduced kinetic model investigated in this work yields a readily discernible representation of metastable states within the phase space of the molecular system. Numerical experiments demonstrate how effectively the proposed method discovers interpretable and accurate low-dimensional representations of given full-state kinetics from simulations.

I. INTRODUCTION

As one of the basic tasks of analysis of molecular dynamics (MD) simulations, model reduction is important for understanding the kinetics of molecular systems, which aims to find a small number of observables of the molecular configuration, usually called reaction coordinate (RC), and projects the original molecular kinetics to the space of RC. An ideal RC is a sufficient statistics which can accurately predict the evolution of configurations in future, so that the reduced kinetics of RC can preserve essential part of the full-state kinetics.

Because the manual selection of RCs heavily relies on prior knowledge of molecular systems and requires repeated trial-and-errors in applications, a lot of data-driven methods for model reduction have been proposed in the past decade. According to transfer operator theory, we can select slow variables with large time-lagged correlations as RCs for molecular systems with fast-slow time scale separation¹⁻⁵. For example, the well-established time-lagged independent component analysis (TICA) method^{6,7}, which is similar to the dynamic mode decomposition in the field of dynamical systems⁸, represents slow variables by linear transformations of the original molecular coordinates. It is shown in⁹ that TICA and its nonlinear extensions¹⁰⁻¹⁵ can be considered as special cases of the variational approach for Markov processes (VAMP), and several deep learning based methods have been proposed within the VAMP framework¹⁶⁻¹⁹. However, in the case where there is no significant time scale gap, it is difficult to obtain effective low-dimensional description of the molecular kinetics by collecting all slow components. In order to alleviate this problem, some model reduction methods, which directly minimize the prediction errors of future configurations (or configuration distributions) for given RCs by deep learning or kernel machines, have been proposed. Examples include the time-lagged autoencoder²⁰, transition manifold method^{21,22}, and past-future information bottleneck

method²³. Moreover, for investigation of transitions between the specific reactant and product states of a molecular system, RC can also be obtained from the committor function^{24,25}.

After obtaining RC, the reduced kinetics along RC can be represented by a stochastic governing equation according to the theory of effective dynamics^{26,27}, but the computation and analysis of the equation are usually infeasible for high-dimensional molecular systems. Some recent modeling methods of dynamical systems can discover RC with a simple governing equation of the reduced kinetics by assuming the existence of the inverse function from RC to the system state^{28,29}. However, these methods are not applicable to MD simulations, where the assumption does not hold and the conditional distribution of the molecular configuration for given RC is generally intractable (see discussion in Section II A).

In this work, we introduce an innovative model reduction technique based on normalizing flow (NF), called RC flow, which enables the simultaneous discovery of nonlinear reaction coordinate transformations and the modeling of corresponding reduced kinetics. Normalizing Flows (NFs) are a class of invertible neural network known for their capacity to perform explicit density estimation on high-dimensional data³⁰, which have also proven to be effective tools for modeling and predicting equilibrium distributions in molecular systems³¹⁻³⁷, as well as in other many-body systems^{38,39}. Notably, in the Timewarp method recently proposed by Klein et al.⁴⁰, NFs have demonstrated remarkable proficiency in constructing transferable kinetic models for molecular systems over extended timescales. Our method utilizes an NF to decompose the full-state configuration coordinate into RC and white noise independent of kinetics, then the surrogate model of the full-state molecular kinetics can be explicitly reconstructed from the governing equation of RC due to the invertibility of NF. We model the governing equation by Brownian dynamics for interpretability and tractability of the reduced kinetics, and all parameters of the

NF and Brownian dynamics can be obtained via maximum likelihood estimation from simulation data. RC flow stands out as an ideal choice for molecular kinetics model reduction, distinguished by several unique traits:

- It introduces a scalable approach to model reduction that extends beyond the traditional framework of identifying slow variables. In contrast to conventional methods, which solely focus on locating slow variables, RC flow enables the collaborative description of multiple dominant components of molecular kinetics through more effective and small-sized RCs.
- RC flow enables simultaneous training of coordinate transformations and reduced kinetics, and the model of reduced kinetics can be specified according to practical requirements.
- The Brownian dynamics-based reduced kinetic model considered in this work can furnish a clear and low-dimensional depiction of metastable states within the phase space of the molecular system.

Several numerical tests are presented to illustrate the effectiveness of the RC flow.

II. BACKGROUND

A. Reaction coordinate

In MD simulations, the time evolution of a molecular system can be considered as a Markov process $\{\mathbf{x}_t\}$ in a high-dimensional configuration space contained in \mathbb{R}^D , and the molecular kinetics can be fully described by the transition density $p_\tau^x(\mathbf{x}, \mathbf{y}) = \mathbb{P}(\mathbf{x}_{t+\tau} = \mathbf{y} | \mathbf{x}_t = \mathbf{x})$, where \mathbf{x}_t denotes the system configuration at time t . Furthermore, we assume in this paper that the MD simulation is performed without applying any external force and the time-reversibility

$$\mu^x(\mathbf{x})p_\tau^x(\mathbf{x}, \mathbf{y}) = \mu^x(\mathbf{y})p_\tau^x(\mathbf{y}, \mathbf{x})$$

is fulfilled, where $\mu^x(\mathbf{x})$ represents the equilibrium distribution of the configuration.

If we select RC as $\mathbf{z}_t = \Phi(\mathbf{x}_t) \in \mathbb{R}^d$ with $d \ll D$ and model the kinetics embedded in the RC space by the transition density $p_\tau^z(\mathbf{z}_t, \mathbf{z}_{t+\tau}) = \mathbb{P}(\mathbf{z}_{t+\tau} | \mathbf{z}_t)$, the full-state kinetics can be reconstructed from the reduced kinetics as

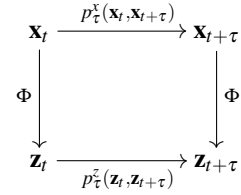
$$\hat{p}_\tau^x(\mathbf{x}_t, \mathbf{x}_{t+\tau}) = \int p_\tau^z(\mathbf{z}_t, \mathbf{z}) \mathbb{P}(\mathbf{x}_{t+\tau} | \Phi(\mathbf{x}_{t+\tau}) = \mathbf{z}) d\mathbf{z}, \quad (1)$$

and the relationship between μ^x and the equilibrium distribution μ^z of RC is provided by

$$\mu^x(\mathbf{x}) = \int \mu^z(\mathbf{z}) \mathbb{P}(\mathbf{x} | \Phi(\mathbf{x}) = \mathbf{z}) d\mathbf{z}, \quad (2)$$

where $\mathbb{P}(\mathbf{x} | \Phi(\mathbf{x}) = \mathbf{z})$ denotes the conditional distribution of the configuration \mathbf{x} for given RC \mathbf{z} .

The relationship between the variables and transition densities is shown in the diagram below:



It can be observed from the diagram that model parameters of the coordinate transformation Φ and the reduced transition density p_τ^z can be fitted by maximizing the likelihood of \hat{p}_τ^x for given simulation trajectories. A major difficulty of such a model reduction procedure arises from the density $\mathbb{P}(\mathbf{x} | \Phi(\mathbf{x}) = \mathbf{z})$ in (1,2), which is a probability distribution over the level set $\{\mathbf{x} | \Phi(\mathbf{x}) = \mathbf{z}\}$ of Φ and is generally intractable for conventional probabilistic models especially for nonlinear Φ . In what follows, we will address this difficulty by using normalizing flows.

B. Normalizing flow

Normalizing flows (NFs) are a specific class of neural networks for modeling distributions of high-dimensional data^{30,41}. For a random variable \mathbf{x} , we can train an NF F so that $\bar{\mathbf{z}} = F(\mathbf{x})$ is distributed according to a tractable distribution, e.g., standard Gaussian distribution $\mathcal{N}(\mathbf{0}, \mathbf{I})$, where F is a bijective function consisting of a sequence of invertible transformations. After training, we can approximate the density of \mathbf{x} as

$$\mathbb{P}(\mathbf{x}) = \mathcal{N}(\bar{\mathbf{z}} | \mathbf{0}, \mathbf{I}) \left| \det \left(\frac{\partial F(\mathbf{x})}{\partial \mathbf{x}} \right) \right| \quad (3)$$

according to the change of variables formula and draw samples from the density by

$$\begin{aligned} \bar{\mathbf{z}} &\sim \mathcal{N}(\mathbf{0}, \mathbf{I}), \\ \mathbf{x} &= F^{-1}(\bar{\mathbf{z}}), \end{aligned} \quad (4)$$

where $\mathcal{N}(\cdot | \mathbf{a}, \Sigma)$ denotes the Gaussian density function with mean \mathbf{a} and covariance matrix Σ . There have been many types of NF models available in literature⁴²⁻⁴⁶. For most models, the Jacobian determinant of F and the inverse F^{-1} in Eqs. (3, 4) can be efficiently calculated due to the specifically designed network structures.

III. REACTION COORDINATE FLOW

A. Model architecture

In this section, we develop a RC flow for model reduction of MD simulation data, which can identify low-dimensional RC and model reduced kinetics simultaneously. The key idea

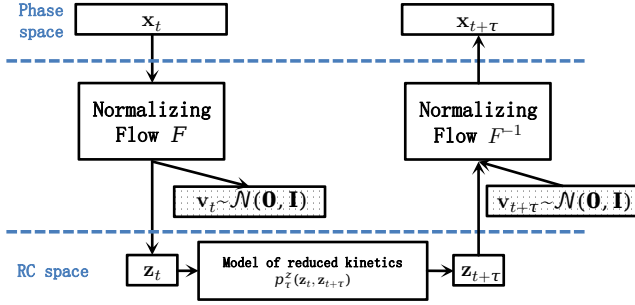


FIG. 1. Diagram of RC flow for model reduction of molecular kinetics. The NF F transforms state \mathbf{x}_t into a vector consisting of the RC \mathbf{z}_t and the noise $\mathbf{v}_t \sim \mathcal{N}(\mathbf{0}, \mathbf{I})$. Correspondingly, $\mathbf{x}_{t+\tau}$ can be reconstructed from $\mathbf{z}_{t+\tau}$ as $\mathbf{x}_{t+\tau} = F^{-1}(\mathbf{z}_{t+\tau}, \mathbf{v}_{t+\tau})$ by sampling $\mathbf{v}_{t+\tau} \sim \mathcal{N}(\mathbf{0}, \mathbf{I})$. The time evolution of \mathbf{z}_t is characterized by Brownian dynamics (9) in this paper.

is to utilize an NF F to decompose the configuration \mathbf{x}_t into RC and noise parts as the following:

$$F(\mathbf{x}_t) = (\mathbf{z}_t, \mathbf{v}_t), \quad (5)$$

where the RC \mathbf{z}_t is governed by a low-dimensional kinetic model and the noise $\mathbf{v}_t \stackrel{\text{iid}}{\sim} \mathcal{N}(\mathbf{0}, \mathbf{I})$ is uninformative in predicting future evolution of configurations. A diagram illustrating the model architecture is shown in Fig. 1.

From the decomposition (5) and the invertibility of F , we can obtain the coordinate transformation

$$\Phi(\mathbf{x}) = [F(\mathbf{x})]_{1,\dots,d}$$

and an analytical expression of the conditional distribution of \mathbf{x} over the \mathbf{z} -level set

$$\begin{aligned} \mathbb{P}(\mathbf{x}|\Phi(\mathbf{x}) = \mathbf{z}) &= \mathbb{P}(\mathbf{z}, \mathbf{v}|\Phi(\mathbf{x}) = \mathbf{z}) \left| \det \left(\frac{\partial F(\mathbf{x})}{\partial \mathbf{x}} \right) \right| \\ &= \delta_{\mathbf{z}}(\Phi(\mathbf{x})) S(\mathbf{x}), \end{aligned} \quad (6)$$

where

$$S(\mathbf{x}) = \mathcal{N}(\mathbf{v}|\mathbf{0}, \mathbf{I}) \left| \det \left(\frac{\partial F(\mathbf{x})}{\partial \mathbf{x}} \right) \right|$$

and $\delta_{\mathbf{z}}$ denotes the Dirac delta distribution centered at \mathbf{z} . By substituting (6) into (1,2), we can recover the full-state thermodynamics and kinetics from the reduced ones as

$$\hat{p}_{\tau}^{\mathbf{x}}(\mathbf{x}_t, \mathbf{x}_{t+\tau}) = p_{\tau}^{\mathbf{z}}(\Phi(\mathbf{x}_t), \Phi(\mathbf{x}_{t+\tau})) S(\mathbf{x}_{t+\tau}) \quad (7)$$

$$\mu^{\mathbf{x}}(\mathbf{x}) = \mu^{\mathbf{z}}(\Phi(\mathbf{x})) S(\mathbf{x}) \quad (8)$$

In RC flow, the reduced kinetics $p_{\tau}^{\mathbf{z}}$ can be modeled by any kind of kinetic model according to the practical requirements. In this paper, we focus on the Brownian dynamics

$$d\mathbf{z}_t = -\nabla V(\mathbf{z}_t) dt + \sqrt{2\beta^{-1}} dW_t, \quad (9)$$

which is widely used in computational chemistry and physics for characterizing diffusion processes in complicated energy

landscapes^{47–49}. Here W_t denotes standard Brownian motion, V is potential function, β is inverse temperature, which we take to be 1 without loss of generality (see Appendix A), and the asymptotic steady-state probability distribution of \mathbf{z}_t is⁵⁰

$$\mu^{\mathbf{z}}(\mathbf{z}) \propto \exp(-V(\mathbf{z})). \quad (10)$$

The closed-form of the transition density $p_{\tau}^{\mathbf{z}}$ of the Brownian dynamics (9) is generally unavailable, but there are many numerical methods that can produce numerical approximations effectively (see survey in⁵¹). In our experiments, we select the importance sampling method proposed in⁵², which is outlined in Appendix E.

Remark 1. Conditional NF can also be used to model $p_{\tau}^{\mathbf{z}}$, as demonstrated in⁴⁰, avoiding the complex numerical computations associated with SDEs. Nevertheless, this approach sacrifices interpretability in reduced kinetics and presents challenges in obtaining the reduced potential of \mathbf{z}_t .

Here, we model F by RealNVP⁴⁴. For $\mu^{\mathbf{z}}$, which is a low-dimensional density and usually multimodal, we select Gaussian mixture model (GMM) in the form of

$$\hat{\mu}^{\mathbf{z}}(\mathbf{z}) = \frac{\sum_{i=1}^{K^d} w(\mathbf{c}_i)}{\sum_{j=1}^{K^d} w(\mathbf{c}_j)} \mathcal{N}(\mathbf{z}|\mathbf{c}_i, \text{diag}(\boldsymbol{\sigma}(\mathbf{c}_i))^2) \quad (11)$$

according to our numerical experience. In (11), centers $\mathbf{c}_1, \dots, \mathbf{c}_{K^d}$ are kept as grid points of a regular grid in the d -dimensional RC space (see Line 9 in Algorithm 1), and $w(\mathbf{c}) \in \mathbb{R}$, $\boldsymbol{\sigma}(\mathbf{c}) \in \mathbb{R}^d$ are considered as functions of centers, which are both represented by multilayer perceptrons with exponential output activation functions. The drift term in the reduced kinetics (9) can then be calculated as

$$-\nabla V = \nabla \log \mu^{\mathbf{z}}.$$

Remark 2. RC flow can also be characterized by parametric models of F and V . But in this case, the calculation of

$$\hat{\mu}^{\mathbf{x}}(\mathbf{x}) = \mu^{\mathbf{z}}(\Phi(\mathbf{x})) S(\mathbf{x}) = \frac{\exp(-V(\Phi(\mathbf{x}))) S(\mathbf{x})}{\int \exp(-V(\mathbf{z})) d\mathbf{z}}$$

involves an intractable integral over the RC space.

B. Loss functions

In order to identify RC that can characterize thermodynamics and kinetics of the molecular system, we consider the following two loss functions for training of RC flow:

Kinetic loss: To recover full-state kinetics from the RC flow, we use the negative log-likelihood (NLL) loss of the estimated transition density

$$\mathcal{L}_{\text{kin}} = -\frac{1}{T-\tau} \sum_{t=1}^{T-\tau} \log \hat{p}_{\tau}^{\mathbf{x}}(\mathbf{x}_t, \mathbf{x}_{t+\tau}) \quad (12)$$

for a given simulation trajectory $\{\mathbf{x}_1, \dots, \mathbf{x}_T\}$, where $\hat{p}_{\tau}^{\mathbf{x}}$ is defined by (7). In the case of multiple trajectories, \mathcal{L}_{kin} can be defined as the average NLL over all transition pairs with lag time τ within all trajectories.

Equilibrium loss: An ideal RC flow also allows an accurate estimation of the steady-state probability distribution, and the estimation error can be achieved using the loss

$$\mathcal{L}_{\text{eq}} = -\frac{1}{T^s} \sum_{t=1}^{T^s} \log \hat{\mu}^x(\mathbf{x}_t^s), \quad (13)$$

where $\hat{\mu}^x$ is given by (8) and $\{\mathbf{x}_1^s, \dots, \mathbf{x}_{T^s}^s\}$ are sampled from the global equilibrium (e.g., from enhanced sampling simulations). In numerical experiments of this paper, MD simulation trajectories are long enough and achieve equilibrium, so we simply set $\{\mathbf{x}_1^s, \dots, \mathbf{x}_{T^s}^s\} = \{\mathbf{x}_1, \dots, \mathbf{x}_T\}$.

Therefore, leaving aside numerical details, we can solve the following problem with weight $\alpha > 0$ to find optimal parameters of the RC flow:

$$\min_{F, \mu^z} \mathcal{L} = \mathcal{L}_{\text{kin}} + \alpha \mathcal{L}_{\text{eq}}, \quad (14)$$

C. Pre-processing and training

It is well-known that the performance of training neural networks can be significantly improved by normalizing the data scales and decoupling the correlation between features of the data. In a previous study³¹, it was also reported that whitening transformation can enhance the performance of learning Boltzmann distributions by normalizing flows (NFs). In this paper, we perform data pre-processing by TICA^{6,7} for large-sized systems and let $\mathbf{x}_t^{\text{TICA}} = \mathbf{W}(\mathbf{x}_t - \bar{\mathbf{x}})$, where $\bar{\mathbf{x}}$ denotes the mean value of the original configuration and \mathbf{W} denotes the transformation matrix given by TICA. If the features of the original configuration x_t are linearly independent, then \mathbf{W} is invertible, and $F(\mathbf{W}(\mathbf{x} - \bar{\mathbf{x}}))$ is still an invertible function with respect to \mathbf{x} . This data pre-processing approach offers several advantages. First, the features of $\mathbf{x}_t^{\text{TICA}}$ are orthonormal with an identity covariance matrix, making them nearly standard Gaussian distributed. Second, the TICA components are sorted according to their relaxation time scales, with the slowest and most important components arranged in the first dimensions. Therefore, $\mathbf{x}_t^{\text{TICA}}$ is already close to an ideal combination of reaction coordinate and noise after the TICA transformation, which simplifies the learning problem. Further details on the TICA can be found in Appendix B.

Based on the above analysis, Algorithm 1 provides a summary of the training process of RC flow. In the algorithm, we first simplify the reduced kinetics as a Brownian motion with $\nabla V(\mathbf{z}) \equiv 0$ and initialize F by minimizing \mathcal{L}_{kin} . Next, we obtain a rectangle area $\prod_{i=1}^d [\text{LB}_i, \text{UB}_i]$ that covers all RCs of training data, locate the K^d centers of the GMM of μ^z uniformly in the area, and initialize the weights and variance matrices by minimizing \mathcal{L} . Last, all parameters of F and μ^z are simultaneously optimized with objective function \mathcal{L} . In our experiments, all the optimization problems involved in the algorithm are solved by the mini-batch Adam algorithm⁵³.

Notice the pre-processing and pre-training steps are included in the algorithm to stabilize the training, and can be

replaced with other heuristic strategies according to practical requirements.

Remark 3. In this paper, the transformation coefficients $\mathbf{W}, \bar{\mathbf{x}}$ obtained by TICA remain unchanged during the training procedure. It is important to note that some recently proposed normalizing flow models (e.g., KRnet⁴⁶) incorporate trainable linear layers with invertible transformation matrices. The application of such NFs to the RC flow framework requires further investigation and evaluation.

Algorithm 1: Training algorithm of RC flow

- 1 **if** data pre-processing is required **then**
- 2 Perform TICA transformation

$$\mathbf{x}_t := \mathbf{W}(\mathbf{x}_t - \bar{\mathbf{x}}) \text{ for all } t.$$

- 3 **end**
- 4 **if** pre-training is required **then**
- 5 Perform pre-training (optional):
- 6 Let $\mu^z(\mathbf{z}) \propto 1$, i.e., $\nabla V(\mathbf{z}) \equiv 0$, and train F with \mathcal{L}_{kin} defined in (12).
- 7 Calculate $(\mathbf{z}_t, \mathbf{v}_t) = F(\mathbf{x}_t)$ for $t = 1, \dots, T$.
- 8 Let

$$\begin{aligned} \text{LB}_i &= \min\{\text{ith element of } \mathbf{z}_t | t = 1, \dots, T\}, \\ \text{UB}_i &= \max\{\text{ith element of } \mathbf{z}_t | t = 1, \dots, T\}. \end{aligned}$$

for $i = 1, \dots, d$.

- 9 Let

$$\{\mathbf{c}_1, \dots, \mathbf{c}_{K^d}\} = \prod_{i=1}^d \left\{ \text{LB}_i + \frac{k(\text{UB}_i - \text{LB}_i)}{K-1} \mid k = 0, \dots, K-1 \right\}$$

- 10 Train $w(\mathbf{c}), \sigma(\mathbf{c})$ with \mathcal{L} defined in (14) while keeping F fixed.
 - 11 **end**
 - 12 Train F and $w(\mathbf{c}), \sigma(\mathbf{c})$ simultaneously with \mathcal{L} .
 - 13 **Return** $F(\cdot)$ (or $F(\mathbf{W}(\cdot - \bar{\mathbf{x}}))$ if Line 2 is implemented).
-

IV. ANALYSIS

A. Spectral analysis

It is well known that the Brownian dynamics (9) is a time-reversible Markov process and its transition density can be decomposed into a set of relaxation processes as^{1,2}

$$p_\tau^z(\mathbf{z}_t, \mathbf{z}_{t+\tau}) = \sum_{i=0}^{\infty} r_i^z(\mathbf{z}_t) \cdot e^{-\frac{\tau}{t_i}} r_i^z(\mathbf{z}_{t+\tau}) \mu^z(\mathbf{z}_{t+\tau}), \quad (15)$$

for all $\tau > 0$, where $t_0 = \infty > t_1 \geq t_2 \geq \dots$ are implied time scales, $r_0^z, r_1^z, r_2^z, \dots$ are eigenfunctions of the transfer operator of $\{\mathbf{z}_t\}$, and $r_0^z(\mathbf{z}) \equiv 1$. If there is a spectral gap and $t_1 \geq \dots \geq t_{s-1} \gg t_s$, we can conclude that the kinetics of $\{\mathbf{z}_t\}$ at large time scales is dominated by the first s relaxation processes.

In the case where the RC flow is well trained and provides an accurate approximation of p_τ^x , it can be proved that

$t_0, t_1, t_2 \dots$ are also implied time scales of $\{\mathbf{x}_t\}$, and we can obtain the dominant eigenfunctions and relaxation processes of $\{\mathbf{x}_t\}$ from those of RC with

$$r_i^x(\mathbf{x}) = r_i^z(\Phi(\mathbf{x})) \quad (16)$$

and

$$p_\tau^x(\mathbf{x}_t, \mathbf{x}_{t+\tau}) = \sum_{i=0}^{\infty} r_i^x(\mathbf{x}_t) \cdot e^{-\frac{\tau}{t_i}} r_i^x(\mathbf{x}_{t+\tau}) \mu^x(\mathbf{x}_{t+\tau}). \quad (17)$$

The detailed derivations of the above conclusions are given in Appendix C.

B. RC flow and information bottleneck

One important metric to evaluate the quality of RC is the mutual information $MI(\mathbf{z}_t, \mathbf{x}_{t+\tau})$, which quantifies the statistical dependence between \mathbf{z}_t and $\mathbf{x}_{t+\tau}$. According to the principle of past–future information bottleneck^{23,54}, if \mathbf{z}_t is an ideal bottleneck variable with large mutual information, it can accurately predict the future evolution of the configuration.

For RC flow, it can be established that, as the size of simulation data tends towards infinity, the following inequality holds:

$$MI(\mathbf{z}_t, \mathbf{x}_{t+\tau}) \geq -\mathcal{L}_{\text{kin}} + \text{const.}, \quad (18)$$

where the constant is independent of our model parameters. Detailed proof of this result is provided in Appendix D. Thus, RC flow can also be interpreted as an information bottleneck method, which maximizes a lower bound of the mutual information $MI(\mathbf{z}_t, \mathbf{x}_{t+\tau})$ with a specific kinetic model of \mathbf{z}_t .

V. NUMERICAL EXAMPLES

In this section, we apply RC flow to model reduction of some diffusion processes with multiple metastable states and the alanine dipeptide, where F is modeled by a realNVP. All the model and implementation details are presented in Appendix F.

First, we consider Brownian dynamics driven by the double well potential and the Mueller potential as shown in Fig. 2A, and use RC flow to identify the one-dimensional RC z based on simulation trajectories in the configuration space of $\mathbf{x} = (x_1, x_2)$. Fig. 2B plots the reduced potential V of z , which can be divided into several potential wells by barriers. We also present in Fig. 2A full-state configurations belonging to different potential wells through the inverse mapping $\mathbf{x} = F^{-1}(z, 0)$ for $z \in \mathbb{R}$. It can be seen that RCs identified by the RC flow can preserve the structure of metastable states, and the stationary distributions of RCs are accurately estimated. In addition, we utilize Markov state models (MSMs)^{55,56} to estimate the dominant implied time scales of the processes from the original simulation trajectories of \mathbf{x} and trajectories of RC generated by (9). The results are given in Fig. 2C,

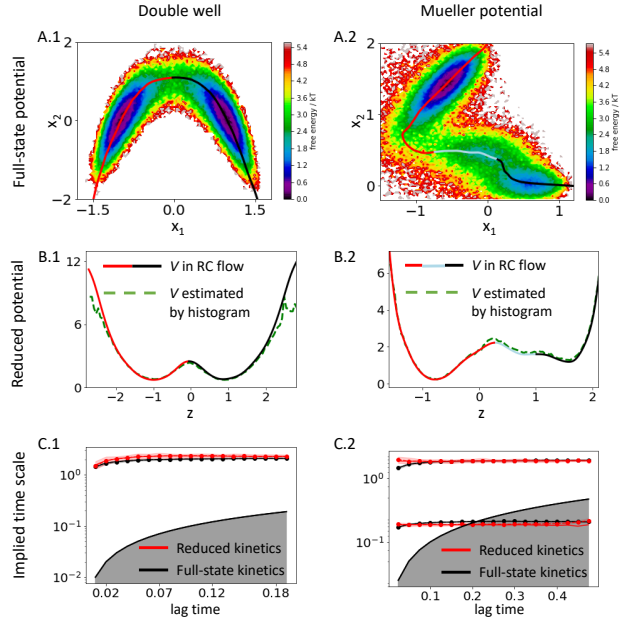


FIG. 2. Model reduction of two-dimensional diffusion processes. (A) Potential energy functions in \mathbb{R}^2 . The solid lines consist of points $\{F^{-1}(z, 0) | z \in \mathbb{R}\}$, and points with the same colors indicate they belong to the same potential well of the reduced potential V . (B) Reduced potentials of RCs. The solid lines represent V estimated by the GMM in RC flow, where the potential wells are created by local maxima of V , and the dash lines represent potentials estimated by the histogram of $\{z_t\}$. (C) Dominant implied time scales of the reduced kinetics (9) of z_t (red) and the full-state Brownian dynamics of \mathbf{x}_t (black), which are both calculated from simulation trajectories by the MSM approach at different lag times (see Appendix F 3 for details of calculation).

which demonstrate the consistency between the full-state and reduced kinetics.

As a second example, the data are generated by a diffusion process with potential

$$V^s(\mathbf{s}) = V'(s_1, s_2) + 10s_3^2,$$

where $\mathbf{s} = (s_1, s_2, s_3)$ is the state, the potential V' of (s_1, s_2) plotted in Fig. 3A has seven wells, and s_3 evolves as an independent Ornstein-Uhlenbeck process with equilibrium distribution $\mathcal{N}(s_3 | 0, 0.05)$ and the mixing time much smaller than that of (s_1, s_2) . In this example, the true simulation data of \mathbf{s} are mapped to $\mathbf{x} = (x_1, x_2, x_3)$ lying around a “Swiss roll” manifold by a nonlinear transformation as shown in Fig. 3B, and the RC flow is implemented to find a two-dimensional RC. Figs. 3C and 3D reveal that the proposed method successfully “unfolds” the manifold of simulation data and the kinetic properties of the process are preserved under the model reduction.

Last, we use RC flow to analyze simulation data of alanine dipeptide. This molecular system has been extensively studied in the existing literature, and its kinetics on long timescales can be characterized by two dihedral angles ϕ, ψ of the backbone (Fig. 4A). Here we perform model reduction to find a two-dimensional RC with the configuration $\mathbf{x} \in \mathbb{R}^{30}$

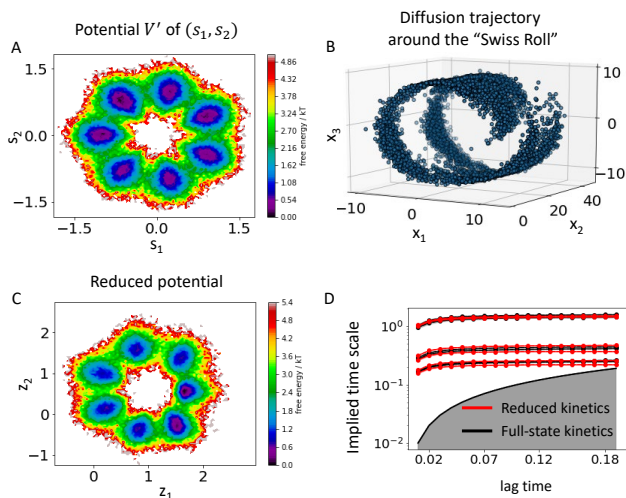


FIG. 3. Model reduction of the diffusion process around a “Swiss roll”. (A) Circular potential V' of (s_1, s_2) (see Appendix F 2). (B) Diffusion trajectory of $\mathbf{x} = (x_1, x_2, x_3)$ obtained by the transformation (F1). (C) Reduced potential of $\mathbf{z} = (z_1, z_2)$ obtained by RC flow. (D) Dominant implied time scales t_1, \dots, t_6 of the reduced kinetics (9) of \mathbf{z}_t (red) and the full-state Brownian dynamics of \mathbf{x}_t (black), which are calculated by the MSM approach at different lag times.

being Cartesian coordinates of heavy atoms. From Fig. 4B, we can see that the free energy landscape of dihedral angles (ϕ, ψ) is close to that of \mathbf{z} identified by RC flow. We further grouped molecular configurations into six macro-states based on potential wells of (ϕ, ψ) , and the macro-states can also be separated in the space of \mathbf{z} (Fig. 4C). In addition, Fig. 4D shows that the largest three implied time scales of the reduced kinetics provided by RC flow are close to those calculated from MSMs in the space of (ϕ, ψ) .

VI. CONCLUSIONS

Model reduction of molecular kinetics, including discovery of RC and projection of kinetics into RC space, is an important task in analyzing and simulating molecular systems, and RC flow proposed in this paper provides a novel data-driven approach to the task. By harnessing the invertibility of NF, RC flow makes it tractable to compute conditional distributions of configurations based on specified RCs. Consequently, the reconstruction of full-state thermodynamics and kinetics from the reduced model becomes a straightforward process. Remarkably, within the RC flow framework, the optimization of coordinate transformations and the modeling of reduced kinetics can be simultaneously executed. Furthermore, it offers the flexibility to select from various governing equations for RCs in alignment with practical requirements.

In future, we will focus on the applications of RC flows to adaptive sampling and transition path finding methods, and the following open problems require further investigations:

- A rigorous mathematical analysis of modeling errors of RC flows under some proper assumptions (e.g.,

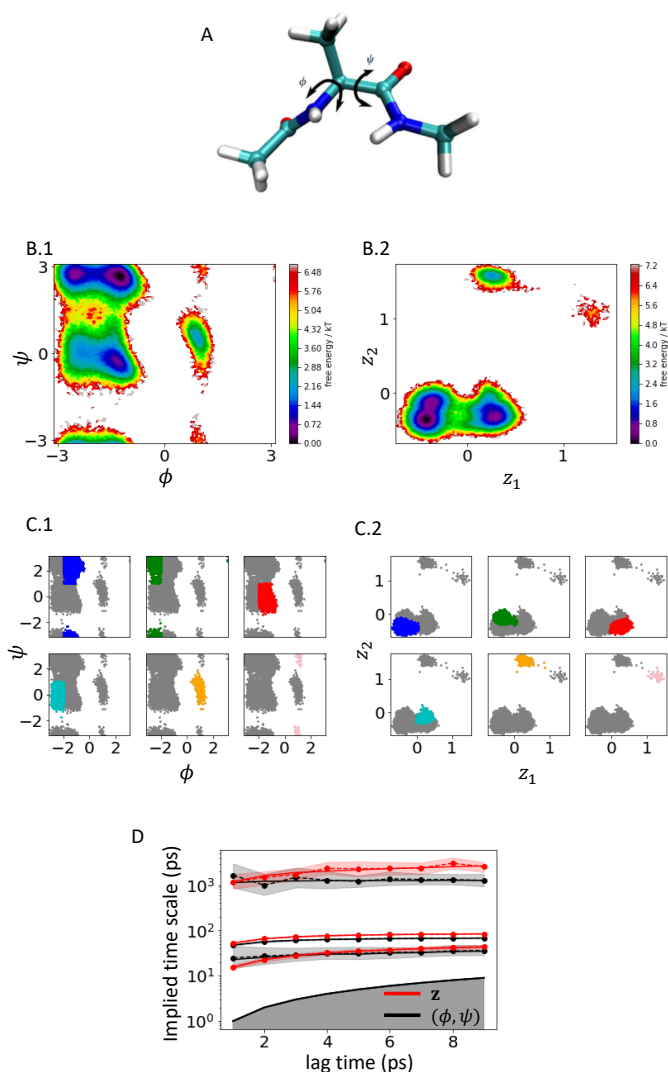


FIG. 4. Model reduction of alanine dipeptide. (A) Structure of alanine dipeptide. The main coordinates are the backbone torsion angles ϕ and ψ . (B) Reduced potential of (ϕ, ψ) and $V(\mathbf{z})$ given by the RC flow. (C) Macro-states defined in the space of (ϕ, ψ) and their projections in the space of \mathbf{z} . (D) Implied timescales t_1, t_2, t_3 of the reduced kinetics provided by the RC flow (red), and those estimated from MD simulation trajectories in the space of (ϕ, ψ) (black).

existence of low-dimensional transition manifold²¹) would be desirable.

- In common model reduction methods, large lag times τ are usually selected to achieve effective low-dimensional description of kinetics especially for long time scales. But for RC flows, the accurate and efficient calculation of the transition density $p_{\tau}^z(\mathbf{z}_t, \mathbf{z}_{t+\tau})$ of the reduced kinetics with a large τ is still challenging.

Appendix A: Analysis of the inverse temperature

For a RC flow given by (5) and (9) with $\beta \neq 1$, we can define a new RC \mathbf{z}'_t as

$$F'(\mathbf{x}_t) = (\mathbf{z}'_t, \mathbf{v}_t) = (\sqrt{\beta} \mathbf{z}_t, \mathbf{v}_t), \quad (\text{A1})$$

where F' is also an invertible function. Substituting (A1) into (9) yields

$$d\mathbf{z}'_t = -\nabla V'(\mathbf{z}'_t) dt + \sqrt{2} dW_t \quad (\text{A2})$$

with

$$V'(\mathbf{z}') = \beta V(\sqrt{\beta^{-1}} \mathbf{z}').$$

It can be seen that (A1, A2) provide an equivalent RC flow with the inverse temperature of the reduced kinetics being 1.

Appendix B: Data pre-processing

For completeness, we introduce the TICA-based data pre-processing approach. The interested readers can refer to^{6,7} for further discussion and implementation guidance.

Suppose we are given a trajectory $\mathbf{x}_1, \dots, \mathbf{x}_T$ of length T and lag time Δt . For notational simplicity, we denote the mean value of \mathbf{x}_t by $\bar{\mathbf{x}}$, the difference between \mathbf{x}_t and $\bar{\mathbf{x}}$ by $\delta \mathbf{x}_t = \mathbf{x}_t - \bar{\mathbf{x}}$, and the projection of \mathbf{x}_t onto the TICA space by $\mathbf{x}_t^{\text{TICA}}$. TICA solves the following optimization problems iteratively for $i = 1, 2, \dots$,

$$\max_{\mathbf{w}_i} \text{auto}(\mathbf{w}_i, \Delta t) = \mathbf{w}_i^\top \mathbf{C}(\Delta t) \mathbf{w}_i$$

subject to constraints $\mathbf{w}_i^\top \mathbf{C}(0) \mathbf{w}_i = 1$ and $\mathbf{w}_i^\top \mathbf{C}(0) \mathbf{w}_j = 0$ for $j = 1, \dots, i-1$. Here, $\mathbf{C}(0)$ and $\mathbf{C}(\Delta t)$ are the estimated covariance and time-lagged covariance matrices of \mathbf{x}_t given by

$$\begin{aligned} \mathbf{C}(0) &= \frac{1}{T} \sum_t \delta \mathbf{x}_t \delta \mathbf{x}_t^\top, \\ \mathbf{C}(\Delta t) &= \frac{1}{2(T-\Delta t)} \sum_t \left(\delta \mathbf{x}_t \delta \mathbf{x}_{t+\Delta t}^\top + \delta \mathbf{x}_{t+\Delta t} \delta \mathbf{x}_t^\top \right). \end{aligned}$$

$\text{auto}(\mathbf{w}_i, \Delta t)$ denotes the autocorrelation of the component $\mathbf{w}_i^\top \mathbf{x}_t$ with lag time Δt , and the largest autocorrelations yield the slowest components. By combining all optimal \mathbf{w}_i , we can obtain the TICA transformation

$$\mathbf{x}_t^{\text{TICA}} = \mathbf{W}(\mathbf{x}_t - \bar{\mathbf{x}})$$

with $\mathbf{W} = (\mathbf{w}_1, \mathbf{w}_2, \dots)^\top$, which ensures that $\mathbf{x}_t^{\text{TICA}}$ has zero mean and identity covariance. In this paper, we use the function `pyemma.coordinates.tica` in the Python package `PyEMMA`⁵⁷ to implement the TICA transformation.

In the case where $\mathbf{C}(0)$ is full-rank, $\mathbf{W} \in \mathbb{R}^{D \times D}$ is an invertible matrix. Adopting TICA for data pre-processing ensures that the mapping $(\mathbf{z}_t, \mathbf{v}_t) = F(\mathbf{x}_t^{\text{TICA}}) = F(\mathbf{W}(\mathbf{x}_t - \bar{\mathbf{x}}))$ given by RC flow is still invertible with respect to \mathbf{x}_t . We can

then reconstruct the original configuration \mathbf{x}_t from the RC \mathbf{z}_t and noise \mathbf{v}_t as

$$\begin{aligned} \mathbf{x}_t &= \mathbf{W}^{-1} \mathbf{x}_t^{\text{TICA}} + \bar{\mathbf{x}} \\ &= \mathbf{W}^{-1} F^{-1}(\mathbf{z}_t, \mathbf{v}_t) + \bar{\mathbf{x}}. \end{aligned}$$

However, if \mathbf{x}_t contains linearly dependent elements and $\mathbf{C}(0)$ is numerically singular, TICA removes the linear dependence and provides \mathbf{W} with row number smaller than D . In this case, we can obtain an approximate inverse mapping from $(\mathbf{z}_t, \mathbf{v}_t)$ to \mathbf{x}_t by minimizing the error $\|\delta \mathbf{x}_t - \widehat{\mathbf{W}}^{-1} \mathbf{x}_t^{\text{TICA}}\|^2 = \|\delta \mathbf{x}_t - \widehat{\mathbf{W}}^{-1} \mathbf{W} \delta \mathbf{x}_t\|^2$, which yields

$$\widehat{\mathbf{W}}^{-1} = \delta \mathbf{X} (\mathbf{W} \delta \mathbf{X})^+.$$

Here $\delta \mathbf{X} = (\delta \mathbf{x}_1, \dots, \delta \mathbf{x}_T)$ and the superscript $+$ denotes the Moore-Penrose pseudo inverse. Finally, we can approximately reconstruct configuration \mathbf{x}_t from $(\mathbf{z}_t, \mathbf{v}_t)$ by

$$\mathbf{x}_t \approx \widehat{\mathbf{W}}^{-1} F^{-1}(\mathbf{z}_t, \mathbf{v}_t) + \bar{\mathbf{x}}.$$

Appendix C: Transfer operators of $\{\mathbf{x}_t\}$ and $\{\mathbf{z}_t\}$

We first briefly introduce properties of the transfer operator \mathcal{T}_τ^z of (9), which is defined by

$$\mathcal{T}_\tau^z h(\mathbf{z}) = \int \frac{\mu^z(\mathbf{z}')}{\mu^z(\mathbf{z})} p_\tau^z(\mathbf{z}', \mathbf{z}) h(\mathbf{z}') d\mathbf{z}', \text{ for } \langle h, h \rangle_{\mu^z} < \infty.$$

For more details, we refer to⁴ and references therein. Due to the time-reversibility of the Brownian dynamics, \mathcal{T}_τ^z is a self-adjoint operator and can be written in terms of the eigenfunctions as

$$\mathcal{T}_\tau^z h = \sum_{i=0}^{\infty} \lambda_i^\tau \langle h, r_i^z \rangle_{\mu^z} r_i^z$$

Here $1 = \lambda_0^\tau > \lambda_1^\tau \geq \lambda_2^\tau \geq \dots$ are eigenvalues, which are associated with implied time scales as $t_i = -\tau / \log(\lambda_i^\tau)$, $r_0^z = \mu^z$, r_1^z, r_2^z, \dots are normalized eigenfunctions with $\langle r_i^z, r_j^z \rangle_{\mu^z} = 1_{i=j}$, and the inner product $\langle h, h' \rangle_{\mu^z} = \int h(\mathbf{z}) h'(\mathbf{z}) \mu^z(\mathbf{z}) d\mathbf{z}$. Then, we have

$$\begin{aligned} p_\tau^z(\mathbf{z}', \mathbf{z}) &= \frac{\mu^z(\mathbf{z})}{\mu^z(\mathbf{z}')} \mathcal{T}_\tau^z \delta_{\mathbf{z}'}(\mathbf{z}) \\ &= \frac{\mu^z(\mathbf{z})}{\mu^z(\mathbf{z}')} \sum_{i=0}^{\infty} \lambda_i^\tau \mu^z(\mathbf{z}') r_i^z(\mathbf{z}') r_i^z(\mathbf{z}) \\ &= \sum_{i=0}^{\infty} r_i^z(\mathbf{z}') \cdot \lambda_i^\tau r_i^z(\mathbf{z}) \mu^z(\mathbf{z}) \end{aligned}$$

Next, we prove that (17) holds for RC flow. According to the decomposition of p_τ^z and (7),

$$\begin{aligned} p_\tau^x(\mathbf{x}', \mathbf{x}) &= p_\tau^z(\mathbf{z}', \mathbf{z}) S(\mathbf{x}) \\ &= \sum_{i=0}^{\infty} r_i^z(\mathbf{z}') \cdot \lambda_i^\tau r_i^z(\mathbf{z}) \mu^z(\mathbf{z}) S(\mathbf{x}) \\ &= \sum_{i=0}^{\infty} r_i^x(\mathbf{x}') \cdot \lambda_i^\tau r_i^x(\mathbf{x}) \mu^z(\mathbf{x}), \end{aligned}$$

where $F(\mathbf{x}) = (\mathbf{z}, \mathbf{v})$, $F(\mathbf{x}') = (\mathbf{z}', \mathbf{v}')$ and $r_i^x(\mathbf{x}) = r_i^z(\Phi(\mathbf{x}))$.

Moreover, based on the above analysis, the eigendecomposition of the transfer operator of $\{\mathbf{x}_t\}$ can be written as

$$\begin{aligned} \mathcal{T}_\tau^x h(\mathbf{x}) &\triangleq \int \frac{\mu^x(\mathbf{x}')}{\mu^x(\mathbf{x})} p_\tau^x(\mathbf{x}', \mathbf{x}) h(\mathbf{x}') d\mathbf{x}' \\ &= \sum_{i=0}^{\infty} \int r_i^x(\mathbf{x}') h(\mathbf{x}') \mu^x(\mathbf{x}') d\mathbf{x}' \cdot \lambda_i^\tau r_i^x(\mathbf{x}) \\ &= \sum_{i=0}^{\infty} \lambda_i^\tau \langle h, r_i^x \rangle_{\mu^x} r_i^x(\mathbf{x}). \end{aligned}$$

By considering

$$\begin{aligned} \langle r_i^x, r_j^x \rangle_{\mu^x} &= \int r_i^x(\mathbf{x}) r_j^x(\mathbf{x}) \mu^x(\mathbf{x}) d\mathbf{x} \\ &= \iint r_i^z(\mathbf{z}) r_j^z(\mathbf{z}) \mu^z(\mathbf{z}) \mathcal{N}(\mathbf{v}|\mathbf{0}, \mathbf{I}) d\mathbf{z} d\mathbf{v} \\ &= \langle r_i^z, r_j^z \rangle_{\mu^z} \\ &= \mathbf{1}_{i=j}, \end{aligned}$$

we can conclude that $\mathcal{T}_\tau^x r_i^x = \lambda_i^\tau r_i^x$, i.e., λ_i^τ and $r_i^x(\mathbf{x}) = r_i^z(\Phi(\mathbf{x}))$ are the i th eigenvalue and eigenfunction of \mathcal{T}_τ^x .

Appendix D: Proof of (18)

We show here the derivation of (18) for the self-completeness of the paper. The similar proof can be found in²³.

For convenience of notation, we denote by

$$\hat{\mathbb{P}}(\mathbf{x}_{t+\tau}|\mathbf{z}_t) = p_\tau^z(\mathbf{z}_t, \Phi(\mathbf{x}_{t+\tau})) S(\mathbf{x}_{t+\tau})$$

the approximation of the conditional distribution $\mathbb{P}(\mathbf{x}_{t+\tau}|\mathbf{z}_t)$ given by RC flow. It can be seen from (7) that $\hat{\mathbb{P}}(\mathbf{x}_{t+\tau}|\mathbf{z}_t) = \hat{p}_\tau^x(\mathbf{x}_t, \mathbf{x}_{t+\tau})$ in RC flow. According to the definition of mutual information, we have

$$\begin{aligned} \text{MI}(\mathbf{z}_t, \mathbf{x}_{t+\tau}) &= \mathbb{E}[\log \mathbb{P}(\mathbf{x}_{t+\tau}|\mathbf{z}_t)] + H(\mathbf{x}_{t+\tau}) \\ &= \mathbb{E} \left[\log \frac{\mathbb{P}(\mathbf{x}_{t+\tau}|\mathbf{z}_t)}{\hat{\mathbb{P}}(\mathbf{x}_{t+\tau}|\mathbf{z}_t)} \right] + \mathbb{E}[\log \hat{\mathbb{P}}(\mathbf{x}_{t+\tau}|\mathbf{z}_t)] \\ &\quad + H(\mathbf{x}_{t+\tau}) \\ &= \mathbb{E}_{\mathbf{z}_t} \left[\mathbb{E}_{\mathbf{x}_{t+\tau} \sim \mathbb{P}(\mathbf{x}_{t+\tau}|\mathbf{z}_t)} \left[\log \frac{\mathbb{P}(\mathbf{x}_{t+\tau}|\mathbf{z}_t)}{\hat{\mathbb{P}}(\mathbf{x}_{t+\tau}|\mathbf{z}_t)} \right] \middle| \mathbf{z}_t \right] \\ &\quad + \mathbb{E}[\log \hat{p}_\tau^x(\mathbf{x}_t, \mathbf{x}_{t+\tau})] + H(\mathbf{x}_{t+\tau}) \end{aligned}$$

where H denotes the entropy and \mathbb{E} denotes the mean value over all transition pairs $(\mathbf{x}_t, \mathbf{x}_{t+\tau})$ in trajectories. Notice that $\mathbb{E}_{\mathbf{x}_{t+\tau} \sim \mathbb{P}(\mathbf{x}_{t+\tau}|\mathbf{z}_t)} \left[\log \frac{\mathbb{P}(\mathbf{x}_{t+\tau}|\mathbf{z}_t)}{\hat{\mathbb{P}}(\mathbf{x}_{t+\tau}|\mathbf{z}_t)} \right]$ equals the KL divergence between $\mathbb{P}(\mathbf{x}_{t+\tau}|\mathbf{z}_t)$ and $\hat{\mathbb{P}}(\mathbf{x}_{t+\tau}|\mathbf{z}_t)$, which is always non-negative. Therefore, in the limit case of infinite data size, we can obtain

$$\mathbb{E}[\log \hat{\mathbb{P}}(\mathbf{x}_{t+\tau}|\mathbf{z}_t)] = -\mathcal{L}_{\text{kin}}$$

and

$$\text{MI}(\mathbf{z}_t, \mathbf{x}_{t+\tau}) \geq -\mathcal{L}_{\text{kin}} + H(\mathbf{x}_{t+\tau}),$$

where the last term is independent of parameters of RC flow. The equality holds only if $\hat{\mathbb{P}}(\mathbf{x}_{t+\tau}|\mathbf{z}_t) = \mathbb{P}(\mathbf{x}_{t+\tau}|\mathbf{z}_t)$.

Appendix E: Calculation of p_τ^z

In the importance sampling method⁵², the time interval $[t, t + \tau]$ is divided into M sub-intervals of length $\Delta = \tau/M$. Letting $\mathbf{u}_0 = \mathbf{z}_t$, $\mathbf{u}_1 = \mathbf{z}_{t+\Delta}$, ..., $\mathbf{u}_M = \mathbf{z}_{t+M\Delta} = \mathbf{z}_{t+\tau}$ and applying Euler-Maruyama discretization to each sub-interval, we have

$$\begin{aligned} p_\tau^z(\mathbf{z}_t, \mathbf{z}_{t+\tau}) &= \int \mathbb{P}(\mathbf{u}_1|\mathbf{u}_0) \dots \mathbb{P}(\mathbf{u}_M|\mathbf{u}_{M-1}) d\mathbf{u}_{1:M-1} \\ &= \int f(\mathbf{u}_0, \mathbf{u}_1) \dots f(\mathbf{u}_{M-1}, \mathbf{u}_M) d\mathbf{u}_{1:M-1}, \end{aligned} \quad (\text{E1})$$

where $\mathbf{u}_{1:M-1} = (u_1, \dots, u_{M-1})$ and

$$f(\mathbf{u}, \mathbf{u}') = \mathcal{N}(\mathbf{u}'|\mathbf{u} - \nabla V(\mathbf{u}) \cdot \Delta, 2\Delta \mathbf{I}).$$

According to⁵², We can draw K_s samples of $\mathbf{u}_{1:M-1}$ from the proposal density

$$\mathbf{u}_{1:M-1}^k \sim \prod_{m=0}^{M-2} g_m(\mathbf{u}_m^k, \mathbf{u}_{m+1}^k), \quad \text{for } k = 1, \dots, K_s$$

and calculate the integral (E1) by importance sampling

$$p_\tau^z(\mathbf{z}_t, \mathbf{z}_{t+\tau}) \approx \frac{1}{K_s} \sum_{k=1}^{K_s} \frac{\prod_{m=0}^{M-1} f(\mathbf{u}_m^k, \mathbf{u}_{m+1}^k)}{\prod_{m=0}^{M-2} g_m(\mathbf{u}_m^k, \mathbf{u}_{m+1}^k)} \quad (\text{E2})$$

where $\mathbf{u}_0^k \equiv \mathbf{u}_0 = \mathbf{z}_t$, $\mathbf{u}_M^k \equiv \mathbf{u}_M = \mathbf{z}_{t+\tau}$, and

$$g_m(\mathbf{u}, \mathbf{u}') = \mathcal{N} \left(\mathbf{u}' \middle| \mathbf{u} + \frac{\mathbf{u}_M - \mathbf{u}}{M - m}, \frac{2\Delta(M - m - 1)}{M - m} \mathbf{I} \right). \quad (\text{E3})$$

The whole procedure of the approximation of p_τ^z is summarized in Algorithm 2.

Algorithm 2: Importance sampling approximation of $p_\tau^z(\mathbf{z}_t, \mathbf{z}_{t+\tau})$

- 1 **for** $k = 1, \dots, K_s$ **do**
 - 2 **for** $m = 1, \dots, M - 1$ **do**
 - 3 Draw $\mathbf{u}_m^k \sim g_m(\mathbf{u}_{m-1}^k, \cdot)$ with (E3).
 - 4 **end**
 - 5 **end**
 - 6 Calculate $p_\tau^z(\mathbf{z}_t, \mathbf{z}_{t+\tau})$ by (E2).
-

Appendix F: Model and implementation details

1. Structure and hyperparameters of RC flow

In this work, the RealNVP model of F is implemented in the Bgflow package⁵⁸. It consists of 12 affine coupling

blocks, where shift and scale transformations are performed by multiple layer perceptrons (MLPs) with 3 hidden layers of width 128. In the GMM (11) of μ^z , $w(\mathbf{c})$ and $\sigma(\mathbf{c})$ are modeled by MLPs with 3 hidden layers of width 64, and $K = 40$. The weight α in (14) is set to be 0.1.

In Algorithm 1, Lines 6, 10 and 12 are implemented by Adam algorithm⁵³. Models are trained for 5 epochs (Lines 6 and 10) and 20 epochs (Line 12), and the learning rate is initially 10^{-3} . Moreover, the learning rate is decayed by a factor of 0.1 for every 5 epochs when solving the optimization problem in Line 12. In Algorithm 2, $K_s = 20$ and $M = 10$.

For all our experiments, we implemented pre-training steps. Furthermore, we applied TICA transformations specifically to the examples shown in Figs. 3 and 4 with a lag time of 10 steps.

2. Simulations

Potential functions of examples shown in Fig. 2 are

$$V_{\text{double well}}(x_1, x_2) = 5(x_1^2 - 1)^2 + 10(x_1^2 + x_2 - 1)^2,$$

$$V_{\text{Mueller}}(x_1, x_2) = \sum_{i=1}^4 A_i \exp\left(a_i(x_1 - \bar{x}_i)^2 + b_i(x_1 - \bar{x}_i)(x_2 - \bar{y}_i) + c_i(x_2 - \bar{y}_i)^2\right),$$

where $(A_1, \dots, A_4) = (-\frac{20}{3}, -\frac{10}{3}, -\frac{17}{3}, \frac{1}{2})$, $(a_1, \dots, a_4) = (-1, -1, -6.5, 0.7)$, $(b_1, \dots, b_4) = (0, 0, 11, 0.6)$, $(c_1, \dots, c_4) = (-10, -10, -6.5, 0.7)$, $(\bar{x}_1, \dots, \bar{x}_4) = (1, 0, -0.5, -1)$ and $(\bar{y}_1, \dots, \bar{y}_4) = (0, 0.5, 1.5, 1)$. For each potential, we generate a trajectory containing 1.5×10^5 frames by Euler-Maruyama discretization of the Brownian dynamics with the inverse temperature 0.5 (double well potential) or 1 (Mueller potential). The time intervals between frames and step sizes of the discretization are 0.01, 2×10^{-4} (double well potential) and 0.025, 5×10^{-4} (Mueller potential).

For the example illustrated by Fig. 3, $V'(s_1, s_2) = \cos(7 \cdot \text{atan2}(s_2, s_1))$. The trajectory of \mathbf{s} containing 3×10^5 frames is also generated by the Euler-Maruyama scheme, where the inverse temperature is 1, the time interval between frames is 0.01 and the discretization step size is 2×10^{-4} . The simulation data in the space of \mathbf{x} are obtained via the transformation

$$\begin{aligned} x_1 &= s'_1 \cos s'_1 + \frac{u_1}{\sqrt{u_1^2 + u_3^2}} s_3, \\ x_2 &= s'_2, \\ x_3 &= s'_1 \sin s'_1 + \frac{u_3}{\sqrt{u_1^2 + u_3^2}} s_3, \end{aligned} \quad (\text{F1})$$

where $u_1 = \sin s'_1 + s'_1 \cos s'_1$, $u_3 = -\cos s'_1 + s'_1 \sin s'_1$, $s'_1 = 3\pi(s_1 + 4)/4$ and $s'_2 = 3\pi(s_2 + 4)/4$.

3. Calculation of implied time scales

In our examples, implied time scales are all calculated by 50-state Markov state models built by pyEMMA, where the spatial discretization is performed by k-means clustering. Implied time scales of full-state kinetics are obtained from simulation trajectories in the space of \mathbf{x} (two well and Mueller potentials), \mathbf{s} (Swiss roll), and (ϕ, ψ) (alanine dipeptide). For reduced kinetics defined by (9), implied time scales are obtained from trajectories with the same sizes as training data, which are also generated by the Euler-Maruyama discretization of (9).

- ¹F. Noé and F. Nuske, *Multiscale Modeling & Simulation* **11**, 635 (2013).
- ²F. Nuske, B. G. Keller, G. Pérez-Hernández, A. S. Mey, and F. Noé, *Journal of chemical theory and computation* **10**, 1739 (2014).
- ³S. Klus, P. Koltai, and C. Schütte, *Journal of Computational Dynamics* **3**, 51 (2016).
- ⁴S. Klus, F. Nuske, P. Koltai, H. Wu, I. Kevrekidis, C. Schütte, and F. Noé, *Journal of Nonlinear Science* **28**, 985 (2018).
- ⁵K. A. Kononov, I. C. Unarta, S. Cao, E. C. Goonetilleke, and X. Huang, *JACS Au* **1**, 1330 (2021).
- ⁶G. Pérez-Hernández, F. Paul, T. Giorgino, G. De Fabritiis, and F. Noé, *The Journal of chemical physics* **139**, 07B604_1 (2013).
- ⁷C. R. Schwantes and V. S. Pande, *Journal of chemical theory and computation* **9**, 2000 (2013).
- ⁸I. Mezić, *Nonlinear Dynamics* **41**, 309 (2005).
- ⁹H. Wu and F. Noé, *Journal of Nonlinear Science* **30**, 23 (2020).
- ¹⁰L. Boninsegna, G. Gobbo, F. Noé, and C. Clementi, *Journal of chemical theory and computation* **11**, 5947 (2015).
- ¹¹M. O. Williams, I. G. Kevrekidis, and C. W. Rowley, *Journal of Nonlinear Science* **25**, 1307 (2015).
- ¹²C. R. Schwantes and V. S. Pande, *Journal of chemical theory and computation* **11**, 600 (2015).
- ¹³F. Nuske, R. Schneider, F. Vitalini, and F. Noé, *The Journal of chemical physics* **144**, 054105 (2016).
- ¹⁴H. Wu, F. Nuske, F. Paul, S. Klus, P. Koltai, and F. Noé, *The Journal of chemical physics* **146**, 154104 (2017).
- ¹⁵M. K. Scherer, B. E. Husic, M. Hoffmann, F. Paul, H. Wu, and F. Noé, *The Journal of chemical physics* **150**, 194108 (2019).
- ¹⁶A. Maradt, L. Pasquali, H. Wu, and F. Noé, *Nature communications* **9**, 1 (2018).
- ¹⁷H. Sidky, W. Chen, and A. L. Ferguson, *The Journal of Physical Chemistry B* **123**, 7999 (2019).
- ¹⁸L. Bonati, G. Piccini, and M. Parrinello, *Proceedings of the National Academy of Sciences* **118**, e2113533118 (2021).
- ¹⁹M. Ghorbani, S. Prasad, J. B. Klauda, and B. R. Brooks, *The Journal of Chemical Physics* **156**, 184103 (2022).
- ²⁰C. Wehmeyer and F. Noé, *The Journal of chemical physics* **148**, 241703 (2018).
- ²¹A. Bittracher, P. Koltai, S. Klus, R. Banisch, M. Dellnitz, and C. Schütte, *Journal of nonlinear science* **28**, 471 (2018).
- ²²A. Bittracher, S. Klus, B. Hamzi, P. Koltai, and C. Schütte, *Journal of Nonlinear Science* **31**, 1 (2021).
- ²³Y. Wang, J. M. L. Ribeiro, and P. Tiwary, *Nature communications* **10**, 1 (2019).
- ²⁴Z. D. Pozun, K. Hansen, D. Sheppard, M. Rupp, K.-R. Müller, and G. Henkelman, *The Journal of chemical physics* **136**, 174101 (2012).
- ²⁵J. Lu and E. Vanden-Eijnden, *The Journal of chemical physics* **141**, 07B619_1 (2014).
- ²⁶F. Legoll and T. Lelièvre, *Nonlinearity* **23**, 2131 (2010).
- ²⁷W. Zhang, C. Hartmann, and C. Schütte, *Faraday discussions* **195**, 365 (2016).
- ²⁸B. Lusch, J. N. Kutz, and S. L. Brunton, *Nature communications* **9**, 1 (2018).
- ²⁹K. Champion, B. Lusch, J. N. Kutz, and S. L. Brunton, *Proceedings of the National Academy of Sciences* **116**, 22445 (2019).

- ³⁰I. Kobyzev, S. J. Prince, and M. A. Brubaker, *IEEE transactions on pattern analysis and machine intelligence* **43**, 3964 (2020).
- ³¹F. Noé, S. Olsson, J. Köhler, and H. Wu, *Science* **365**, eaaw1147 (2019).
- ³²H. Wu, J. Köhler, and F. Noé, *Advances in Neural Information Processing Systems* **33**, 5933 (2020).
- ³³J. Köhler, L. Klein, and F. Noé, in *International conference on machine learning* (PMLR, 2020) pp. 5361–5370.
- ³⁴J. Köhler, A. Krämer, and F. Noé, *Advances in Neural Information Processing Systems* **34**, 2796 (2021).
- ³⁵M. Invernizzi, A. Krämer, C. Clementi, and F. Noé, *The Journal of Physical Chemistry Letters* **13**, 11643 (2022).
- ³⁶M. Dibak, L. Klein, A. Krämer, and F. Noé, *Physical Review Research* **4**, L042005 (2022).
- ³⁷J. Köhler, M. Invernizzi, P. De Haan, and F. Noé, arXiv preprint arXiv:2301.11355 (2023).
- ³⁸S.-H. Li and L. Wang, *Physical review letters* **121**, 260601 (2018).
- ³⁹G. Kanwar, M. S. Albergo, D. Boyda, K. Cranmer, D. C. Hackett, S. Racaniere, D. J. Rezende, and P. E. Shanahan, *Physical Review Letters* **125**, 121601 (2020).
- ⁴⁰L. Klein, A. Y. Foong, T. E. Fjelde, B. Mlodozieniec, M. Brockschmidt, S. Nowozin, F. Noé, and R. Tomioka, arXiv preprint arXiv:2302.01170 (2023).
- ⁴¹G. Papamakarios, E. T. Nalisnick, D. J. Rezende, S. Mohamed, and B. Lakshminarayanan, *J. Mach. Learn. Res.* **22**, 1 (2021).
- ⁴²L. Dinh, D. Krueger, and Y. Bengio, arXiv preprint arXiv:1410.8516 (2014).
- ⁴³D. Rezende and S. Mohamed, in *International conference on machine learning* (PMLR, 2015) pp. 1530–1538.
- ⁴⁴L. Dinh, J. Sohl-Dickstein, and S. Bengio, arXiv preprint arXiv:1605.08803 (2016).
- ⁴⁵W. Grathwohl, R. T. Chen, J. Bettencourt, I. Sutskever, and D. Duvenaud, in *International Conference on Learning Representations* (2018).
- ⁴⁶K. Tang, X. Wan, and Q. Liao, *Theoretical and Applied Mechanics Letters* **10**, 143 (2020).
- ⁴⁷W. Ren, E. Vanden-Eijnden, *et al.*, arXiv preprint cond-mat/020528 (2002).
- ⁴⁸N. Singhal, C. D. Snow, and V. S. Pande, *The Journal of chemical physics* **121**, 415 (2004).
- ⁴⁹D. H. Anderson, *Compartmental modeling and tracer kinetics*, Vol. 50 (Springer Science & Business Media, 2013).
- ⁵⁰H. Risken, *The Fokker-Planck Equation* (Springer, 1996).
- ⁵¹B. Jensen and R. Poulsen, *The Journal of Derivatives* **9**, 18 (2002).
- ⁵²G. B. Durham and A. R. Gallant, *Journal of Business & Economic Statistics* **20**, 297 (2002).
- ⁵³D. P. Kingma and J. Ba, arXiv preprint arXiv:1412.6980 (2014).
- ⁵⁴S. Still, *Entropy* **16**, 968 (2014).
- ⁵⁵J.-H. Prinz, H. Wu, M. Sarich, B. Keller, M. Senne, M. Held, J. D. Chodera, C. Schütte, and F. Noé, *The Journal of chemical physics* **134** (2011).
- ⁵⁶B. E. Husic and V. S. Pande, *Journal of the American Chemical Society* **140**, 2386 (2018).
- ⁵⁷M. K. Scherer, B. Trendelkamp-Schroer, F. Paul, G. Pérez-Hernández, M. Hoffmann, N. Plattner, C. Wehmeyer, J.-H. Prinz, and F. Noé, *Journal of Chemical Theory and Computation* **11**, 5525 (2015).
- ⁵⁸<https://github.com/noegroup/bgflow>.